Atmos. Meas. Tech., 9, 3131–3144, 2016
www.atmos-meas-tech.net/9/3131/2016/
doi:10.5194/amt-9-3131-2016

Atmospheric Measurement Techniques
Open Access
EGU

PHIPS–HALO: the airborne Particle Habit Imaging and Polar Scattering probe – Part 1: Design and operation

Ahmed Abdelmonem[1], Emma Järvinen[1], Denis Duft[1], Edwin Hirst[2], Steffen Vogt[1], Thomas Leisner[1], and Martin Schnaiter[1]

[1]Institute for Meteorology and Climate Research, Karlsruhe Institute of Technology, Karlsruhe, Germany
[2]Centre for Atmospheric and Instrumentation Research, University of Hertfordshire, Hatfield, AL10 9AB, UK

Correspondence to: Ahmed Abdelmonem (ahmed.abdelmonem@kit.edu) and Martin Schnaiter (martin.schnaiter@kit.edu)

Received: 9 February 2016 – Published in Atmos. Meas. Tech. Discuss.: 14 March 2016
Revised: 16 June 2016 – Accepted: 18 June 2016 – Published: 20 July 2016

Abstract. The number and shape of ice crystals present in mixed-phase and ice clouds influence the radiation properties, precipitation occurrence and lifetime of these clouds. Since clouds play a major role in the climate system, influencing the energy budget by scattering sunlight and absorbing heat radiation from the earth, it is necessary to investigate the optical and microphysical properties of cloud particles particularly in situ. The relationship between the microphysics and the single scattering properties of cloud particles is usually obtained by modelling the optical scattering properties from in situ measurements of ice crystal size distributions. The measured size distribution and the assumed particle shape might be erroneous in case of non-spherical ice particles. There is a demand to obtain both information correspondently and simultaneously for individual cloud particles in their natural environment. For evaluating the average scattering phase function as a function of ice particle habit and crystal complexity, in situ measurements are required. To this end we have developed a novel airborne optical sensor (PHIPS-HALO) to measure the optical properties and the corresponding microphysical parameters of individual cloud particles simultaneously. PHIPS-HALO has been tested in the AIDA cloud simulation chamber and deployed in mountain stations as well as research aircraft (HALO and Polar 6). It is a successive version of the laboratory prototype instrument PHIPS-AIDA. In this paper we present the detailed design of PHIPS-HALO, including the detection mechanism, optical design, mechanical construction and aerodynamic characterization.

1 Introduction

Better understanding of the radiative impact of different clouds requires knowledge of the link between the cloud microphysics and the single scattering properties of the cloud particles which are used in radiative transfer models. The existing single scattering models, such as Mie theory, usually use the in situ measurements of the ice crystal size distributions as input for optical scattering calculations. Such calculations assume spherical particles to calculate the size distribution from scattering measurements and vice versa. In the past, sophisticated optical methods for the computation of the single scattering properties were developed and applied to non-axisymmetric and irregularly shaped ice particles. These included exact/near-exact methods like T-matrix methods (e.g. Havemann and Baran, 2001), the finite-difference time-domain method (FDTD) (Yang and Liou, 1999) and discrete-dipole approximation (DDA; Draine and Flatau, 1994; Yurkin and Hoekstra, 2007), or methods based on the geometric optics' approximation (Macke et al., 1996), improved geometric optics (IGO) (Bi et al., 2011; Liu et al., 2013; Yang and Liou, 1996) and ray tracing with diffraction on facets (RTDF; Hesse et al., 2009). Despite all these efforts, discrepancies remain between cloud radiative properties measured by spaceborne and ground-based remote sensing and those driven from in situ measured microphysical properties (Baum et al., 2010).

Interpretations of microphysical parameters of cloud particles are usually based on assumptions about the particle shape. Shcherbakov et al. assumed crystals to be hexagonal columns/plates in their modelling approach to retrieve ice

particle parameters (Shcherbakov, 2013; Shcherbakov et al., 2006a, b). The airborne polar nephelometer (PN) (Crépel et al., 1997; Gayet et al., 1997) measures the scattering function of the ice particles and was used in conjunction with results from the Cloud Particle Imager (CPI) probe (Lawson et al., 2001) to investigate the impact of the ice crystal habits on the radiative properties of cirrus clouds. This could be done only using a statistical approach with assumptions made about the particle shape within an ensemble of randomly oriented particles.

The PN measures the optical and microphysical parameters of cloud particles in the size range from a few to about 500 µm. The probe measures the scattering phase function of an ensemble of cloud particles intersecting a collimated laser beam near the focal point of a paraboloidal mirror. The light scattered from polar angles from 3.49 to 169° is reflected onto a circular array of 33 photodiodes. The acquisition rate is selective between 10 Hz and 5 kHz. The PN was operated parallel to the PHIPS-HALO during AIDA cirrus cloud simulation experiments (Schnaiter et al., 2016). Comparison of measurements revealed a reasonable agreement of the two instruments in laboratory-simulated ice clouds. On the other hand, the CPI records high-definition 2-D digital images of cloud particles in the size range from 3 µm to 2 mm and measures particle size, shape, concentration and individual size distributions for water droplets and ice particles. It has a resolution of 2.3 µm and a maximum frame rate of 400 Hz. PHIPS-HALO is similar to a hybrid of those two instruments (PN and CPI) and is characterized by its ability to combine and correlate the optical and microphysical measurements of individual cloud particles. However, the sample statistics of the PHIPS-HALO imaging system is limited, particularly for high-speed aircraft sampling, due to the very slow sampling rate.

Jourdan et al. (2010) used principle component analysis (PCA) of the scattering phase function measured by the PN together with particle habits revealed by CPI to link the microphysical and shape properties of cloud particles to their single scattering properties. This link required a clustering of the collected results according to optical parameters of particles and is only true for particles with sizes larger than 50 µm, as the optical contribution of small particles could not be determined directly in a mixed-phase cloud. Measurements of particle morphology are done by some airborne in situ instruments like the Cloud and Aerosol Spectrometer with Polarization (CASPOL) and the Small Ice Detector (SID). CASPOL measures light scattered by individual aerosol and cloud particles, of sizes from 0.6 to 50 µm, in the forward (4–12) and backward (168–176°) directions, with an additional polarized detector in the backward direction (Glen and Brooks, 2013, 2014). The particle size is determined by the near-forward scattering using Mie theory, and the asphericity is determined by the comparison of the signals from two back detectors measuring total and cross-polarized intensities. SID3 measures the spatial light scattering pattern of individual aerosol and cloud particles in a forward direction (6–25°) for particle sizes ranging from ∼ 1 to 22 µm (Kaye et al., 2008; Vochezer et al., 2016). The 2-D pattern textures reveal information about the particle roughness as could be shown for laboratory-generated ice clouds and midlatitude mixed-phase and cirrus clouds (Ulanowski et al., 2014; Schnaiter et al., 2016).

Different optical array probes, such as the two-dimensional cloud (2-D-C) probe, the two-dimensional stereo (2-D-S) probe and the Cloud Imaging Probe (CIP) have been used to measure the size, shape, and concentration of cloud particles. The 2-D-C and CIP record the 2-D shadow of the hydrometeor as it passes through a collimated laser beam (Baumgardner et al., 2001; Knollenberg, 1970). The image of the shadow is focused onto a plane containing a linear photodiode array, and the status of the elements of that array is recorded at a rate that permits reconstruction of the image. Compared to 2-D-C and CIP, 2-D-S uses two orthogonal laser beams crossed in the middle of the sample volume and produces two shadowgraphs on two high-speed linear arrays. The overlap region is defined by the two laser beams to improve the sample volume boundaries and sizing of small particles (smaller than 100 µm). The stereo views improve the determination of 3-D properties of some particles (Lawson et al., 2006). These optical array probes require the aircraft speed as an input to evaluate the real particle dimensions and to reconstruct a relevant 2-D image. Holographic imaging is used in the Holographic Detector for Clouds (HOLODEC) to obtain the size, 2-D shadow image and 3-D position of every cloud particle coincident in its particle-size-independent sample volume via digital in-line holography (Fugal et al., 2004).

A direct link between the particle habit and the corresponding microphysical parameters is still lacking, at least for complex shapes. For this reason and for accurate correlation, the microphysical and optical properties of ice crystals have to be measured simultaneously by an in situ instrument.

PHIPS-HALO is one of the novel instruments developed for the German DLR HALO GV-SP aircraft and certified by Gulfstream, USA. The resolution power of both microscope units is about 2 µm. The dual imaging configuration facilitates a 3-D morphology impression of the ice crystals. The scattering unit of PHIPS-HALO allows for the measurement of the polar light scattering function of cloud particles with an angular resolution of 1° for forward scattering directions (from 1 to 10°) and 8° for side and backscattering directions (from 18 to 170°). The development of the airborne version (PHIPS-HALO) involved a number of challenges. The high particle speed which may reach up to 200 m s^{-1} due to the HALO aircraft carrier, for instance, required some special considerations for the aerodynamics and detection mechanism. Data acquisition and storage were required to be included within the same compartment.

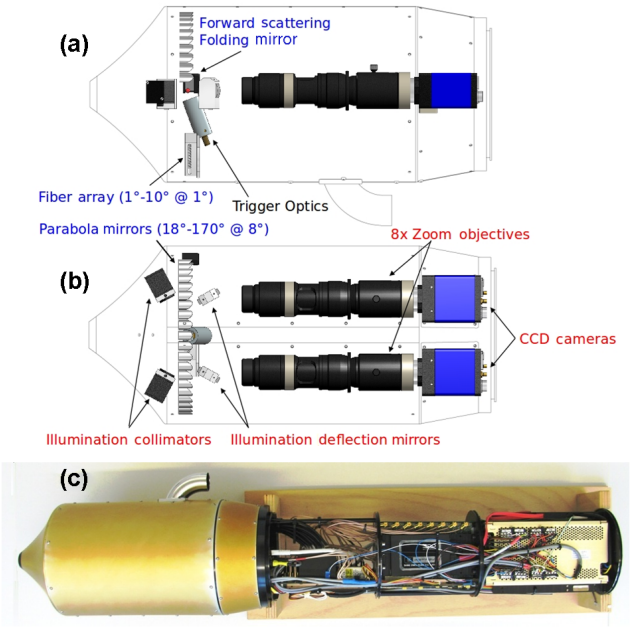

Figure 1. Schematic drawing of the optical detection units used in the PHIPS-HALO probe, **(a)** side view and **(b)** top view. The main components of the polar nephelometer and stereo-microscopic imager are labelled in blue and red, respectively. The trigger optics links the two components. **(c)** A real photo of the probe.

1.1 Basic instrument concept

PHIPS-HALO is the aircraft version of the PHIPS-AIDA laboratory prototype, which is described in detail by Abdelmonem et al. (2011). Both instruments are successive developments of a prototype particle imager (Schön et al., 2011). This prototype particle imager was upgraded with a second identical imaging unit to image the same particle under different viewing angles and by a polar nephelometer for the simultaneous measurement of the single particle angular light scattering function. The basic measurement concept of PHIPS, therefore, is the simultaneous acquisition of stereo images and the angular light scattering function of individual cloud particles. PHIPS-HALO improves upon the other aircraft probes mentioned above with its ability, for the first time, to directly measure the link between the microphysical properties of individual particles and their angular light scattering function. This opens up new opportunities to develop and validate single particle light scattering models based on in situ measurements of atmospheric ice particles.

The basic idea of the instrument is presented in detail in (Abdelmonem et al., 2011) and the basic design of the aircraft version is illustrated in Fig. 1. In brief, the optical head of the probe is composed of two combined optical systems. The polar nephelometer component measures the angular scattered light from individual cloud particles as they intersect a polarized collimated continuous wave laser. Light scattered into the angular range from 1 to 170° with respect to the laser propagation is collected by a specific fibre-based optical system (Sect. 3.1.1.), and is measured by a 32-channel photomultiplier array. One of these channels is used as a trigger input to detect those particles that are in the sensing volume of the instrument. In this way the trigger channel combines the two components of the instrument. The second system is a stereo-microscopic imaging system composed of two identical camera-telescope assemblies (CTAs) and a pulsed illumination laser. The two imaging assemblies are separated by an angular distance of 120° to image the same particle from two directions. With this approach, 3-D information about the particle shape and its orientation with respect to the scattering laser can be inferred. The particles are illuminated by the flash laser using Y-like fibre optics and two optical collimators. Bright field micrographs of the particle are imaged on the charge-coupled device (CCD) of each camera. Both optical systems are controlled by an electronic assembly. This electronic assembly (i) triggers the light scattering measurement and image acquisition, and (ii) processes the scattering signals. The electronic assembly is described in Sect. 3.2.

The major difference between the aircraft and laboratory versions is the compact, light and streamline design of the aircraft version. In addition, a compact electronic assembly, specially developed by the University of Hertfordshire, UK, is used to control the optical systems of PHIPS-HALO. Other important differences are mentioned below within the context of the discussion.

2 Set-up

2.1 Optical head

All structural parts of PHIPS-HALO are made of aluminum AA6060 or AA7075. The covering parts of the optical head are made of DURAL sheet metal (AA2024). The optical head has a cylindrical shape, with an outer diameter of 203 mm and a length of 465 mm. The sample flow outlet extends the head diameter by 51 mm. The outlet faces the ground when the instrument is attached to the aircraft. The volume of the optical head is divided by the main optical plate to which different components are attached. The stereo-microscopic imaging system and the air outlet tube are fixed on one side of the main optical plate, while the trigger detector, the scattering laser and the flash laser are fixed on the other side. The front part of the optical head includes a specially designed inlet. It has a clear diameter of 30 mm at the frontmost of the inlet and 32 mm at the detection volume side and a length of 98 mm. The main task of this inlet is to transfer cloud elements to the sensing area of PHIPS-HALO with a minimum disturbance of their thermodynamic state. All optical components are heated to temperatures above the dew point to prevent water condensation on optics or ice aggregation which may clog the air path.

2.1.1 PHIPS-HALO polar nephelometer

The polar nephelometer, Fig. 1, consists of the front optical ring, back optical ring, 20 off-axis parabolic mirrors (Kaleido Technology, EFL = 15, CA = 10 mm), 20 individual fibre couplers, a forward scattering mirror, a forward scattering coupler for 10 fibres, 30 PMMA (Polymethyl methacrylate) optical fibres of 600 µm diameter and 0.39 numerical aperture (not included in drawings for clarity), a scattering laser beam steerer, trigger optics and a scattering laser source. The scattering laser is a frequency-doubled Nd : YAG laser (CrystaLaser, model CL532-300-L) with a wavelength of 532 nm, an output power of 300 mW, a beam waist of 0.36 mm, a beam divergence of 2 mrad and a beam pointing stability of less than 0.02 mrad. The emitted radiation is linearly polarized with a polarization direction vertical to the base plate of the laser head. The plane of scattering of the polar nephelometer is perpendicular to the main optical plate and includes the centre of scattering of the detection volume which is 20 mm above the optical plate and coincides with the central axis of the inlet tube. The scattering plane is a virtual plane lying between the two optical rings at a distance of 10 mm from the back optical ring, and includes the scattering centre and the off-axis parabolic mirrors. The off-axis parabolic mirrors, which replace the collimating lenses in the laboratory version, are fixed to the optical ring and have their field of view at the detection volume. The CW green laser beam of the scattering laser source is steered to the imaging plane, by a beam steerer fixed between the two rings, and travels along the axis of intersection between the plane of imaging and the plane of scattering. The beam passes through the detection volume to the forward mirror and is then reflected to a beam dump in the forward scattering coupler which is fixed on the back optical ring. This path defines the 0° of the polar scattering angular distribution. The forward coupler has 10 holes, after the beam dump, positioned at equidistant angular distances of 1° (i.e. from 1 to 10°). It is placed at a scattering distance of 200 mm from the scattering centre. The 20 off-axis parabolic mirrors are placed at equidistant angular distances of 8° (from 18 to 170°) and a scattering distance of 83 mm. They are fixed to the first ring on a virtual arc of 83 mm in diameter. The scattered light sampled at the angles between 18 and 170° is reflected and focused to the fibre couplers by the parabolic mirrors. 30 fibre optics are coupled to the forward coupler and the individual fibre couplers and connected to the multi-anode photomultiplier array (MAPMT, Hamamatsu, model H7260) in the electronic part of the probe.

Optical design calculations were performed to define the specifications of the fibre system that couples the scattered light collected by the polar nephelometer to the MAPMT. These calculations were performed by using the optical engineering software FRED (Photon Engineering, LLC, USA). Based on the results of these calculations, an optimum distance between the fibre end and the off-axis parabolic mirror of 16 mm was found that reduces the focal spot to a reasonably small diameter. Furthermore, the numerical aperture of the off-axis mirrors was specified to be smaller than the numerical aperture of the fibres which is the second requirement for a good coupling. The modelled coupling between the fibre end and the MAPMT is shown in Fig. 2. The optical modelling reveals that a residual crosstalk between the individual channels of about 15 % can be expected, even though the fibres are placed close the protection borosilicate window of the MAPMT. This crosstalk was verified by successively coupling laser light from an integrating sphere into the individual fibres while the remaining fibres were blocked. This test was performed on all of the fibres. The result of this laboratory characterization of the MAPMT is shown in Fig. 3. This result represents the mean of the crosstalk from all channels, which were almost identical.

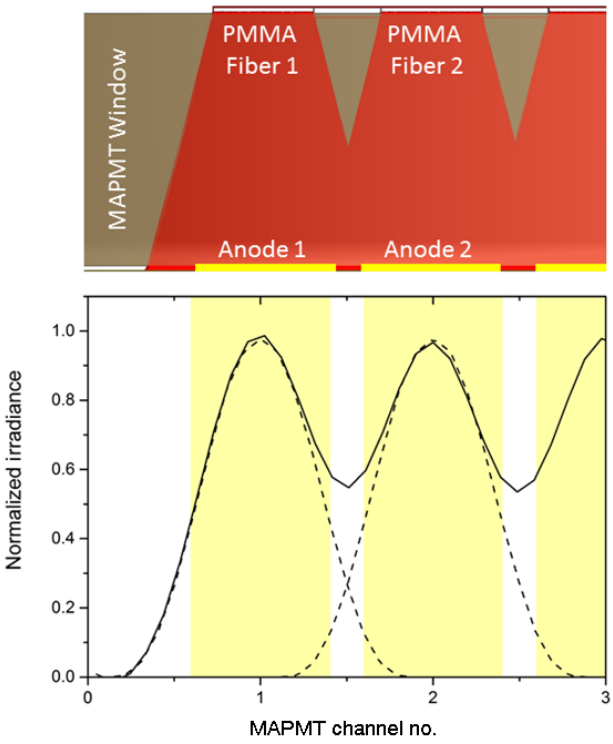

Figure 2. Results of optical modelling calculations for the light coupling between the PMMA fibre system and the multi-anode photomultiplier. A crosstalk of at least 15 % can be expected that needs to be taken into account in the analysis of the polar nephelometer measurements.

To minimize the influence of this crosstalk on the measurement, (i) the fibres are arranged in a respective order, i.e. the angular arrangement is mapped on the MAPMT, and (ii) channel 106° is placed next to the trigger channel (channel 1 of the MAPMT). The latter point is necessary to prevent the instrument from triggering on particles outside of the sensing volume via crosstalk sensitivity. The strong angu-

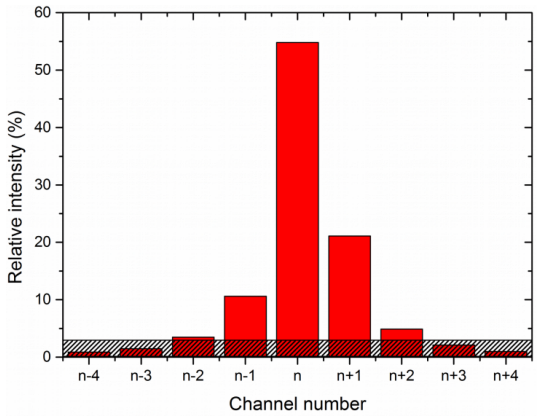

Figure 3. Results of the laboratory characterization of the optical crosstalk within the MAPMT of PHIPS-HALO. The manufacturer-given electronic crosstalk between adjacent detectors of 3 % is indicated by the shaded area. The deduced optical crosstalk between adjacent detectors is 10 % to the left and 20 % to the right side, indicating a slight misplacement of the fibre coupler with respect to the MAPMT.

lar variability of the scattering intensity is shown in Sect. 5, where calculated scattering intensity functions are presented.

2.1.2 Stereo-microscopic imager

Two CTAs are placed downstream of two reflecting mirrors to image the detected particle at two different viewing angles with respect to the particle path inside the probe, i.e. at $+60$ and $-60°$ (in contrast to $+30$ and $-30°$ in the laboratory version) from the central axis of the probe). The imaging plane is defined by the scattering centre and the two CTAs and is perpendicular to the scattering plane. Two identical cameras (GE1380, Allied Vision Technologies Inc., Canada) are used with a 2/3 in. 12 bit CCD sensor, an image resolution of 1360×1024 pixels, a pixel size of 6.45×6.45 µm, a maximum frame rate of 20 Hz, a trigger delay of about 4 µs and a trigger jitter of ±30 ns. Microscopic images are projected onto the CCD sensors by using zoom objectives (Zoom 6000, Navitar Inc., USA) with a variable magnification from 1.4 to 9.0, which corresponds to a field of view ranging from 6.27×4.72 to 0.98×0.73 mm, respectively. The optical resolution ranges from 7.2 to 2.35 µm for the low (1.4×) and high (9.0×) magnification, respectively. A typical operating optical resolution is ∼ 5.3 µm (at 4× magnification) with a field of view of $\sim 2.19 \times 1.65$ mm. The corresponding particle size ranges from ∼ 10 µm to 1.5 mm. The imaging system is calibrated with a calibration slide before each campaign and after any change of the telescope magnification. The objectives have a nominal working distance of 92 mm. The image of a cloud particle is cast on the CCD by freezing the motion of the particle using a 40 ns incoherent pulsed diode laser (Cavitar, model Cavilux, 690 nm, 400 W, Class 4), producing a bright field microscopic image. In contrast to the ultrafast flash lamp used in the prototype version, the incoherent flash laser improves the homogeneity of the image background and the quality of the image due to the high pointing and power stabilities, and prevents chromatic aberrations. The incoherency prevents formation of interference patterns at the CCD. A long-pass filter (THORLABS, FEL0600) is used to prevent the scattered light from disturbing the captured images. The incoherent flash laser and its controller are attached to the optical plate on the other side of the CTAs. The illumination light is transmitted to the detection volume using a Y-like optical fibre (2 mm to 2×1 mm in diameter) coupled to a 90° telescope which collimates the light and aligns it along the axis between the detection volume and camera telescope. The particle is reproduced as a bright field microscopic image on the CCD of each camera. The two images for the same particle at two different angles provide an impression of the 3-D morphology similar to the human stereo vision. The reconstruction of the full 3-D shape is possible for regular geometric shapes like rods, columns, plates, etc. (Abdelmonem et al., 2011). In addition, the investigated parameters can be compared and/or averaged. For example, the larger (or smaller) value of particle size deduced from the two corresponding particle perspectives of plates, columns or complex irregular particles (e.g. rosettes and stars) can be selected specifically to reduce the width in the averaged particle size distribution.

Since PHIPS-HALO is a hybrid of the PN and CPI instruments and combines and correlates the optical and microphysical measurements of individual cloud particles, we present a comparison between the polar nephelometer of PHIPS-HALO and the PN instrument in Table 1 and a comparison between the stereo-microscopic imager of PHIPS-HALO and the CPI probe in Table 2.

2.2 Electronics and signal processing

The electronics of PHIPS-HALO comprises the MAPMT and amplifier board, four analogue signal conditioning and 12 bit analogue-to-digital converter boards, as well as the backplane and control board. Particle data acquisition is controlled by an FPGA (field-programmable gate array) controller located on the backplane board, and communication with the host computer takes place via the USB daughter board mounted on the backplane. The FPGA controls all the functions of the electronics. It sequences the control signals to the peak detectors and analogue-to-digital converters when a particle event is triggered and then stores the returned data in the FIFO. At intervals of approximately 0.7 s, the FPGA stores a particle data set irrespective of whether it has been triggered or not. These forced triggered data can be used to obtain a continuous record of the background signals of the polar nephelometer channels. On a real particle event, a signal is generated by the control board to trigger the PHIPS-HALO cameras and the illumination laser. The delay between these two triggers is programmable up to 10 µs to

Table 1. The specifications of the PN component of PHIPS-HALO compared to those of the PN instrument.

	Instrument	
Parameter	PN instrument	PN of PHIPS-HALO
Detection target	Ensemble of cloud particles (water droplets or ice crystals)	Individual cloud particles (water droplets or ice crystals)
Particle size range	Few to 500 µm	Few to a few hundred µm
No. of measuring channels	33	30 + 1 for trigger
Polar angles range and resolution	Range: 3.49–169° Resolution: 0.79° (3.49–9.02°), 1.58° (9.02–10.6°) and 7° (15–169.5°)	Range: 1–170° Resolution: 1° (1–10°) and 8° (18–170°)
Acquisition rate	10 Hz or 5 kHz	9 kHz
Signal coupling	One paraboloidal mirror for all channels. 10 fibres to photodiode for the forward direction; 23 photodiodes for the side and backward directions	10 direct incidence on fibres for the forward direction and 20 off-axis parabolic mirrors and fibres for the side and backward direction

Table 2. Specifications of the stereo-imager component of PHIPS-HALO compared to those of the CPI probe.

	Instrument	
Parameter	CPI probe	Stereo imager of PHIPS-HALO
Imaging	2-D imaging (one camera)	Stereo imaging (two cameras)
Particle size range	3 µm to 2 mm	10 µm to 1.5 mm (typical range at 4× magnification) ∼ 3 µm to ∼ 4.7 mm (depending on magnification)
Resolution	2.3 µm	∼ 2.35 µm (max.)
Maximum frame rate	400 Hz	20 Hz
Image casting	25 ns pulsed laser diode	40 ns pulsed incoherent laser diode

take into account the camera shutter latency. The triggers are disabled when the camera busy signal is activated.

Figure 4 shows the schematics of the signal detection and processing sequence for a valid particle event. When a particle passes the field of view of the trigger channel, a light pulse is generated on channel 1 of the MAPMT. The analogue trigger signal (Fig. 4a) is routed to a comparator that is used to generate a TTL (transistor–transistor logic) trigger for initiating the data acquisition sequence controlled by the FPGA. The comparator checks whether the following conditions are fulfilled by the signal. (i) The signal is above a certain threshold set by the FPGA and (ii) the signal remained above this threshold for a certain time period to be insensitive to glitches. The latter is also set by the FPGA in clock-cycle units of the electronics which is 48 MHz, i.e. about 21 ns. If both conditions are fulfilled, the FPGA receives a valid particle trigger signal. The FPGA then immediately sends a trigger signal to the cameras to open the shutter. As the cameras have reliable trigger latency times of 3.9 µs, a period of at least 4 µs elapses before a second trigger is sent to the flash laser that illuminates the particle with a pulse of 40 ns. The delay between the particle event detection by the electronics and particle imaging results in a relative distance of about 0.7 mm between the positions along the particle trajectory where the scattering and imaging data are taken. However, a significant change of the particle orientation with respect to the scattering plane during this delay is unlikely as this would require unrealistically high particle angular rotation speeds of the order of 1 kHz.

3 Modelling of the aerodynamic properties of the instrument head

As mentioned above, the probe is designed to fly with a speed of 200 m s^{-1} at an altitude of up to 16 km and temperatures below −60 °C. An aerodynamic study was necessary to estimate the mechanical stability of the probe and to verify the geometry for a turbulence-free detection volume. To this end, CFD (computational fluid dynamics) simulations were carried out using ANSYS CFX 15.0 to evaluate the temperature, pressure and velocity distributions inside and outside the probe.

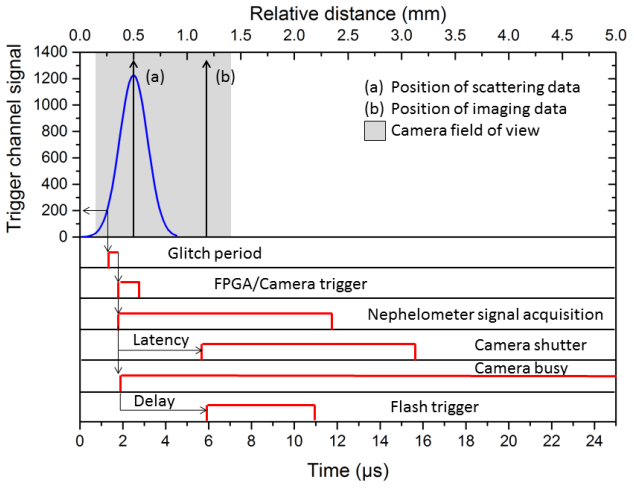

Figure 4. Signal detection and processing scheme for a valid particle event at a typical airspeed of 200 m s^{-1} and at an assumed trigger threshold of 200. The relative distance along the particle trajectory, i.e. the instrument axis, is given on the upper axis. Note, that due to the camera field of view of 1.27 mm along the instrument axis, the imaging system can be aligned in the laboratory by using test particles with particle speeds of only a few metres per second.

To reduce computational effort and improve solution stability, the original complete CAD model of the probe was simplified to include the crucial geometrical features influencing the flow field only. Smaller features, such as screws and cables, as well as objects further away from the open paths, were omitted. Additionally mirror symmetry with respect to the y–z plane was applied. Shear Stress Transport (SST) with automatic wall function and high-speed compressible wall heat transfer option was applied as the turbulence model on a non-buoyant domain using air ideal gas as the fluid. The radial boundary was set as an opening with an activated "zero-gradient turbulence" option. The model was run with input parameters reflecting the range of operation conditions during typical flights of the HALO and Polar 6 aircrafts. The results of a simulation with 187 mbar ambient pressure, 227 K air temperature and 200 m s^{-1} flight speed are shown below.

3.1 Flow velocity and Mach number

To ensure overall stability of the probe and to minimize structural stress on the probe as well as on its mount and the airplane, supersonic speeds of the flow field around the probe should be avoided. Figure 5 shows the modelled Mach number distribution which is the ratio of relative local air speed to the speed of sound inside and outside the probe at a flight speed of 200 m s^{-1}. The simulation shows that Mach numbers are generally below 0.8, with maximum values as high as 0.9 at the outer edges of the probe. However, the speed of sound (MN = 1) is not reached or exceeded.

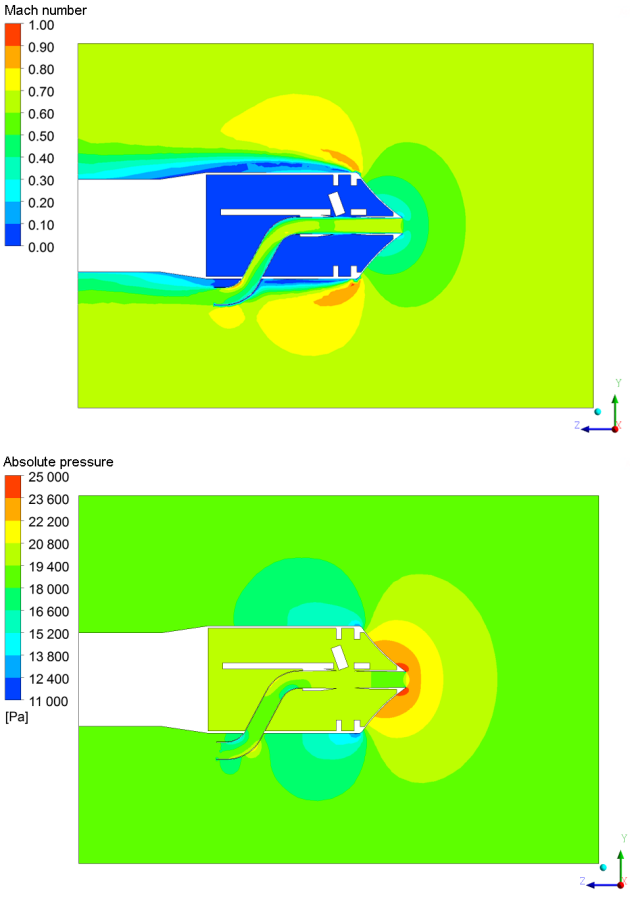

Figure 5. Mach number distribution (upper panel) and pressure distribution (lower panel) of the flow field inside and outside the probe.

The static mechanical stress on the probe can be estimated from the pressure data shown in lower panel of Fig. 5. Due to the open design, the interior of the probe has an overall average pressure elevated by 8 hPa compared to the background pressure. At the probe's front tip and front edge, higher pressure differences of 56 and −79 hPa occur. This is acceptable for the lightweight aluminium structure of the probe under static conditions.

3.2 Temperature

To make sure that pristine and unaltered particles are measured within the detection volume, the temperature along the particle trajectories is important. The temperature distribution inside and outside the probe is shown in the upper panel of Fig. 6. The simulation along the particle trajectory crossing the detection volume in the lower panel shows that the particles experience a short-term temperature change due to adiabatic heating of the surrounding air which lasts for about 1 ms and gives rise to a period of subsaturation and particle evaporation. Basic diffusion growth theory (e.g. Pruppacher and Klett, 1997) can be used to estimate the mass loss for an

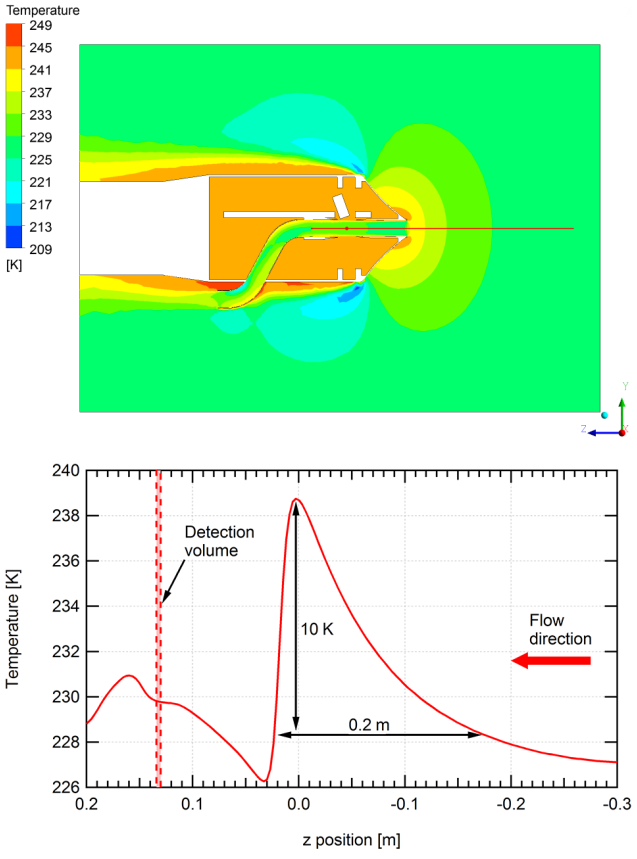

Figure 6. Temperature distribution inside and outside the probe (upper panel) and along the centre line trajectory (lower panel). Incoming particles experience a short-term temperature change of the surrounding air by about 10 K within 1 ms at 200 m s^{-1} flight speed.

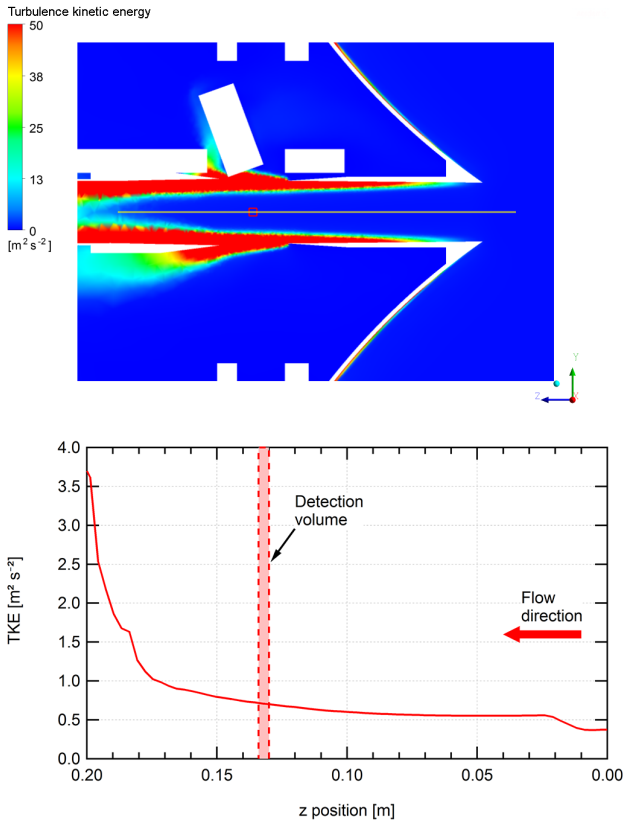

Figure 7. Upper panel: turbulence kinetic energy distribution within the particle flow tube of the probe. The red square marks the detection volume. Lower panel: the TKE along the horizontal centre line trajectory (shown above) is only slightly increased compared to the background value.

ice particle during this period of non-equilibrium conditions. For simplicity, the ice particle is assumed to be spherical for this estimation. The calculation shows that a $d = 2\,\mu$m particle reduces its size by about 5 nm through evaporation, corresponding to a mass loss of $\Delta m/m = 0.8\,\%$, whereas a $d = 10\,\mu$m particle shrinks by less than 1 nm ($\Delta m/m = 0.01\,\%$). This dependence on particle size originates from the fact that due to their larger mass and hence increased heat capacity, larger particles do not accommodate quickly enough to the rapidly changing temperature of the surrounding air. The lower particle temperature directly results in a lower evaporation rate. In conclusion, very small ice particles of $d = 2\,\mu$m and below will experience a short-term evaporation of a few mass percent at the maximum. Larger particles will essentially be unaffected by the short-term heating. The modelled pressure and temperature increases due to compression at the probe tip are in a very good agreement with the values given in Weigel et al. (2015), which are based on temperature, pressure and velocity measurements on the nose boom of the HALO aircraft and the underwing cloud probes.

3.3 Turbulence

Another important parameter for the correct operation of the probe is the degree of turbulence that ice particles experience on their path towards the detection volume. The upper panel of Fig. 7 shows the distribution of turbulence kinetic energy (TKE) which is the kinetic energy per unit mass associated with eddies in turbulent flow. The square root of the TKE is a measure of typical velocities associated with the turbulent fluctuations. The typical turbulent velocity close to the walls of the air channel is about 10 m s^{-1}. This is sufficiently low that potential ice crystals originating from the turbulent region close to the wall do not enter the sample volume and only unperturbed crystals are detected. The TKE along the centre line trajectory is shown in the lower panel of Fig. 7. It reaches a value of about 0.7 m^2 s^{-2} at the detection volume (red square). This corresponds to a typical turbulent velocity of about 0.8 m s^{-1} which should be low enough to not destroy primary, i.e. non-aggregated, cirrus cloud ice crystals.

To verify the operability of the probe under a variety of conditions different from the above scenario, several simula-

Table 3. Simulation results for different model settings corresponding to possible flight conditions. Turbulence kinetic energy at the detection volume (TKE), maximum temperature difference along the centre trajectory (ΔT_{max}) and estimated mass loss due to evaporation ($\Delta m/m$) for three different cloud ice particle diameters.

Flight type	Flight parameters			Results				
	p (bar)	v (m s^{-1})	T (K)	TKE (m^2 s^{-2})	ΔT_{max} (K)	$\Delta m/m$ (%) $d = 2\,\mu$m	$\Delta m/m$ (%) $d = 10\,\mu$m	$\Delta m/m$ (%) $d = 15\,\mu$m
HALO								
Typical	0.187	200	227	0.7	11.8	0.8	0.01	0.003
Low altitude	0.419	110	256	0.2	3.0	1.6	0.04	0.01
High altitude	0.129	240	221	1.7	18.3	1.0	0.01	0.003
Polar 6								
Typical	0.78	75	256	0.06	1.4	0.6	0.02	0.006

tions were performed which reflect the typical range of conditions encountered with the HALO and Polar 6 aircraft. For the operation of the probe, the most important simulation results are the degree of turbulence at the detection volume, the temperature change that cloud particles experience along the trajectories to the detection volume and the estimated mass loss due to evaporation. The results along with the flight parameters are given in Table 3. The first case corresponds to the simulation shown before. The results confirm the conclusions drawn in the analysis above. Turbulence induced by the flow at the probe inlet walls does not propagate to the detection volume due to the speed of air inflow. The degree of turbulence at the detection volume is thus only slightly elevated to the background value under all conditions. The maximum temperature difference that cloud particles experience along their trajectory to the detection volume clearly depends on the speed of the aircraft and is thus highest at the maximum flight speed of 240 m s^{-1} of the HALO aircraft. Nevertheless, even at high speed the mass loss due to evaporation is below 0.1 % for ice particles with a diameter of 10 µm and above.

Ice particle shattering may significantly affect the measurements of any airborne particle probe. The shattering of cloud particles at the inlet of the probe is not discussed here; however, the nozzle of the instrument is designed with a very sharp edge to minimize the probability of collision with that edge. The advantages of a sharp tip and probe-inlet design with respect to minimizing shattering are described in detail by Korolev et al. (2013). Particles hitting the outer part of the tip are forced to follow a trajectory outside the instrument. Shattering caused by collisions with the inner walls of the inlet is largely reduced by the straight design of the inlet. In addition, the inlet has a slowly expanding diameter (from 30 mm at the front tip to 32 mm at the detection volume side) which further reduces the probability of particle shattering.

To evaluate the sensitivity of the probe design to non-zero angle of attack (AoA) conditions, a series of simulations was performed under varying attack angles. It was found that the level of turbulence in the detection volume is not influenced significantly for AoA values below 4°. For higher AoA the level of turbulence in the detection volume increases rapidly, as the turbulence originating from the inlet walls reaches the detection volume. In reality the angle of attack of the HALO aircraft is not constant but depends on air speed and ranges between 1.5 and 6.5° during typical flights, covering low and high altitudes. This range of AoA is compensated partly by a pre-tilted probe mount (2.8° nose down) such that the AoA on the probe is in the range of -1.3 to $+3.7°$, which is well within the limits of ±4°. At the most typical air speed of about 200 m s^{-1}, the AoA on the probe is within ±1°. More details of the AoA study are given in the Supplement.

4 Modelling of the instrument response and detection range for the scattering optics

The PHIPS-HALO probe is designed to image water and ice particles in mixed-phase clouds and ice crystals in cirrus clouds, where the diameter of these particles can range from few to several hundred microns. Simultaneously, the scattering optics measures the scattering phase functions of the imaged particles. The difficulty in the scattering measurements is that a high dynamic range is needed for the detectors, as the intensity of light reaching them can vary several orders of magnitude depending on the laser power, detector geometry and the particle microphysics.

To determine the sensitivity threshold and the dynamic range of the polar nephelometer component of the PHIPS-HALO instrument, we modelled the response of the detectors to scattering by spherical particles. The total power that arrives through the solid angle of a detector from scattering by a sphere with known refractive index is dependent on the incident laser intensity, on the distance of the detector from the scattering centre and on the detector geometry, according

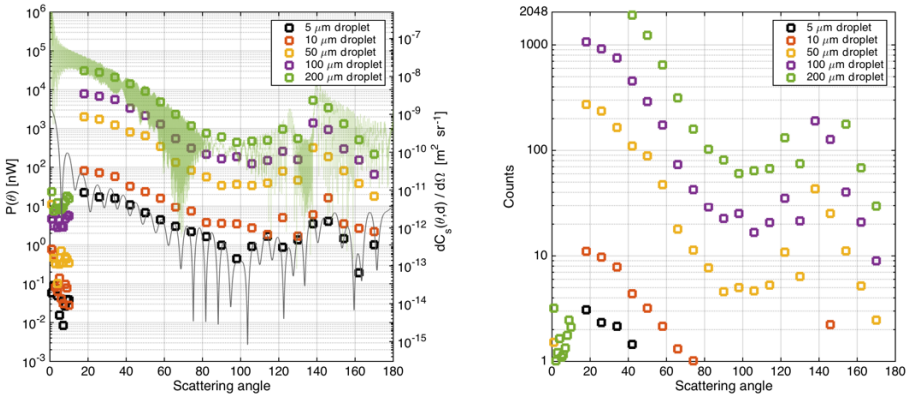

Figure 8. Left: theoretical light power that reaches the detectors by laser light scattering on water droplets with diameters of 5 µm (black squares), 10 µm (orange squares), 50 µm (yellow squares), 100 µm (purple squares) and 200 µm (green squares). For 5 and 200 µm droplets, the scattering cross sections are also shown in high angular resolution. Right: digitized particle scattering functions that are expected for a single MAPMT gain setting.

to the following equation:

$$P(\theta) = \frac{I_0}{4\pi r R^2} \iint\limits_A \frac{\mathrm{d}C_\mathrm{s}}{\mathrm{d}\Omega}(\mathrm{d},\theta)\mathrm{d}\Omega, \quad (1)$$

where I_0 is the laser intensity, R the distance from the scattering centre to the detector, Ω the solid angle of the detector and $\frac{\mathrm{d}C_\mathrm{s}}{\mathrm{d}\Omega}(\mathrm{d}\theta)$ the differential scattering cross section of a particle with a diameter of "d". Since the detector areas are spherical for both forward direction fibres and for the parabolic mirrors in the sideward direction, the double integral (Eq. 1) can be solved analytically with respect to the azimuthal angle. The resulting integral depends on the polar angle only:

$$P(\theta) = 2I_0 \int\limits_{\theta_0-\alpha}^{\theta_0+\alpha} \frac{\mathrm{d}C_\mathrm{s}}{\mathrm{d}\Omega}(\mathrm{d},\theta)\sin\theta \arctan \frac{}{\sqrt{\tan^2\alpha - \tan^2(\theta-\theta_0)}}\mathrm{d}\theta, \quad (2)$$

where α is the half opening angle of the detector ($\arctan(r/R)$). The scattering cross section of the spherical particles can be calculated using Mie theory (the Bohren and Huffman code was used for this; Bohren and Huffman, 2007). For a vertically polarized laser, the scattering cross section can be expressed as follows:

$$\frac{\mathrm{d}C_\mathrm{s}}{\mathrm{d}\Omega}(\mathrm{d}\theta) = \frac{|S_1|^2}{k^2}. \quad (3)$$

The theoretical power measured by a detector (nW) was calculated for five droplets with different diameters (refractive index 1.34 and diameters ranging from 5 to 200 µm) and using a 300 mW laser power with 1 mm diameter and a wavelength of 532 nm. The first 10 forward scattering angles are positioned such that they have 1° resolution at a distance of 200 mm to the scattering centre, and the detectors have a diameter of 0.6 mm. The light scattered to the sideward detectors is gathered with parabolic mirrors (diameter of 10 mm) that have a distance of 83 mm to the scattering centre. The results of the calculations are shown in Fig. 8.

The total scattered intensity measured at a single detector varies by 3 orders of magnitude between a 5 µm and a 200 µm droplet. Additionally, the intensity measured at the 18° detector is 2 orders of magnitude higher than the intensity measured at a 90° angle for the same droplet. The calculation for the differential scattering cross section (black and green solid curves) reveals oscillation features typical of spherical particles. However, these features have a frequency that is significantly higher than the angular resolution of the instrument and, thus, cannot be resolved by the measurements. Larger features, such as the rainbow between 100 and 120° or the decrease in phase function around 100° for a 5 µm droplet and around 130° for 200 µm droplet, can be detected.

Although the MAPMT has a high dynamic range, the electronic processing of the scattering data limits the resolution of the detection to 11 bits. We simulated the possible response to the electronics, assuming ideal optical components with perfect transmission and no crosstalk. The particle size region of interest was chosen to be from 50 µm upwards, since the imaging component will provide more information about the particles at larger particle sizes. We set intensity at the near-90° detector of the 50 µm droplet to be equivalent to five counts (assuming that the MAPMT has a background of few counts) and scaled the scattering responses of other droplets respectively. This would represent one gain setting of the MAPMT. From Fig. 8 we see that the proposed gain setting allowed for the detection of the scattering phase function of 50 and 100 µm droplets over the angular range of 18–170° and the scattering phase function of 200 µm droplets from 42° onwards. In conclusion, we would be able to image and simultaneously measure the scattering phase function of

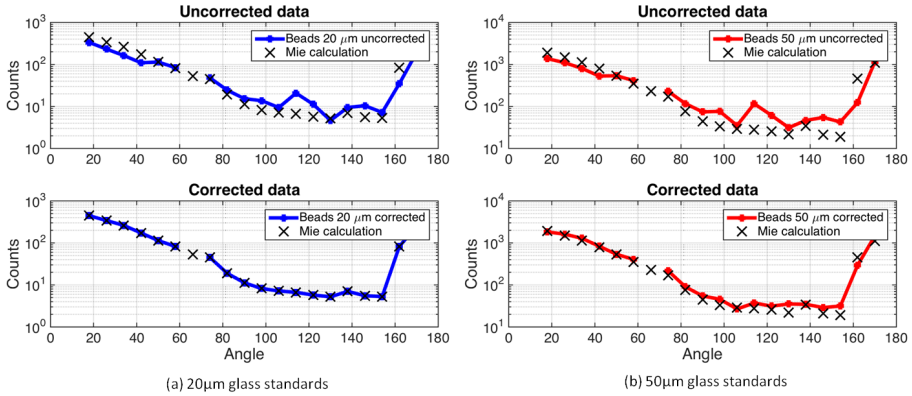

Figure 9. Theoretical (black crosses) and experimental (coloured solid lines) scattering phase functions of two standard glass bead ensembles of 20 µm (blue) and 50 µm (red) diameters. The upper panels show the raw background corrected intensities, and the lower panels show the crosstalk corrected intensities. The missing experimental point at 66° is due to a failure in the corresponding physical channel during the measurement.

particle from 50 µm up to almost 200 µm in diameter. It has to be kept in mind that with ice particles we can expect somewhat flatter scattering phase functions, which would increase the measurement range when measuring in cirrus clouds. By adjusting the MAPMT gain, the measurement range can be shifted to smaller or larger particle sizes.

The forward scattering detectors (1–10°) were positioned at a larger distance from the scattering centre to achieve 1° resolution. The theoretical calculations, however, show that this decreases the intensity in the forward detectors to an extent that the dynamic range of the instrument is not sufficient to measure the low intensities. To improve this, the forward channels would need a separate MAPMT, whose gain can be adjusted independently of the MAPMT for sideward channels, or the forward channels should be brought to the same distance as the sideward detectors, which would mean giving up the 1° resolution.

Characterization of PHIPS-HALO with glass bead measurements

Although this part (Part I) focuses on the design and operation of the probe, we shortly report two sample measurements of standard glass beads which were used for calibration. An ensemble of glass beads (DRI-CAL, Duke Scientific) was dispersed with a home-built particle disperser, consisting of a small glass bulb equipped with inlet and outlet tubing and allowed to pass through the detection volume. The dispersed glass beads were detected by both detection systems. Two standard sizes were used: 19.3 ± 0.7 µm (DC-20) and 49.7 ± 2.0 µm (DC-50). The theoretical scattering phase functions of the given size distributions of the two standards were calculated using Mie theory and integrated over the solid angles of the detectors (black crosses in Fig. 9). The measured scattering phase functions are plotted in solid lines for the 20 µm (blue) and 50 µm (red) glass beads. The upper panels of Fig. 9a and b show the raw background corrected data before the crosstalk corrections. The 20 µm glass beads are used as a reference to define the correction factors for each channel by overlaying the theoretical and measured intensities. We used the 50° as a reference angle and corrected the other measurement angles with respect to it. The correction factors obtained for the individual channels were then used to correct the measured intensities for the 50 µm glass beads (red solid line in the lower panel of Fig. 9b). The good agreement between the corrected measured intensities and the theoretical values of the 50 µm particles validates the crosstalk correction factors.

Although the crosstalk correction factors were determined for spherical particles with a distinct refractive index, it was shown in the study of Schnaiter et al. (2016) that these correction factors also work for ice particles. In that study, the PN of the Université Blaise Pascal, Clermont-Ferrand, France, was operated parallel to the PHIPS-HALO during AIDA cirrus cloud simulation. The PHIPS-HALO data were corrected with the above correction factors, and the comparison of measurements revealed a reasonable agreement of the two instruments in simulated ice clouds.

A collection of processed images from the glass bead measurements used to characterize the scattering component is shown in Fig. 10. The result of the respective image analysis is given in Table 4. For the 50 µm standard, both CTAs show a very good agreement with the manufacturer's specifications, with deviations clearly lying within the uncertainty of the glass bead standard. In case of the 20 µm standard, assembly 2 overestimates the size of the beads by 14 to 19 % which is in agreement with the results by Schön et al. (2011) for this size range and which stems from the image analysis procedure. Assembly 1 oversizes the 20 µm beads by an additional 15 % which can be attributed to the reduced magnification compared to assembly 2. This magnification-dependent oversizing is also shown in Fig. 11.

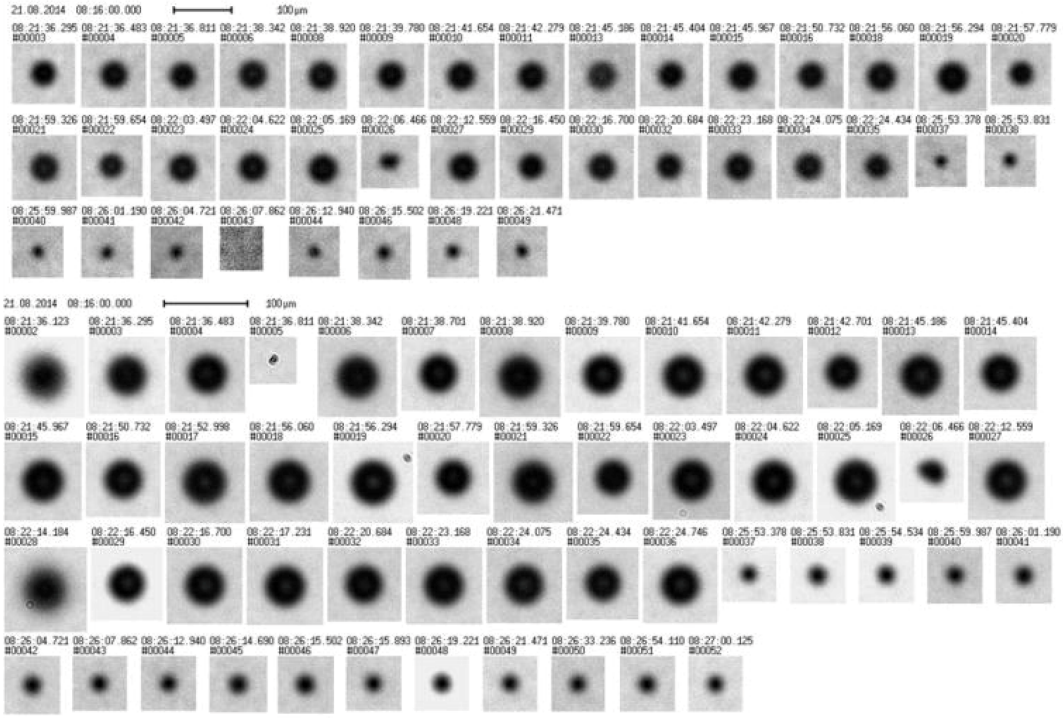

Figure 10. A series of processed images captured by the CTA 1 (4-fold magnification, upper panel) and CTA 2 (6-fold magnification, lower panel) for 50 and 20 µm glass bead standards. Note: less than about 1 % of all images are empty which sometimes is not recognized by the analysis algorithm (image number 43 in the upper panel). These empty images are especially accepted when dirt particles are present on the telescope optics like in the case of image number 5 in the lower panel.

Table 4. Statistical results of the image analysis of glass bead standard measurements. SD denotes standard deviation.

	Manufacturer		Telescope 1 4-fold magnification		Telescope 2 6-fold magnification	
	Mean diameter (µm)	SD (µm)	Mean diameter (µm)	SD (µm)	Mean diameter (µm)	SD (µm)
DRI-CAL 50	49.4 ± 1.6	3.5	49.3	4.1	49.1	4.8
DRI-CAL 20	20.0 ± 0.9	1.9	27.2	1.4	23.9	1.1

5 Summary and outlook

We presented a novel airborne optical probe (PHIPS-HALO) developed at the Karlsruhe Institute of Technology (KIT) for attachment to the German DLR HALO GV-SP aircraft as well as other research aircraft. The probe is unique in its ability to collect two simultaneous and correlated measurements (the 3-D morphology represented in the stereo-image and the corresponding optical properties represented by the polar scattering function) of each individual cloud particle. Hence, PHIPS-HALO provides the missing correlation between the cloud particle habit and its scattering properties which are used in radiative transfer models and can be used as a reference for other airborne cloud-particle probes applied simultaneously during the same flights. In this part (Part I), we focused on the basic concept of the instrument, the design of the optical head, the electronics and signal processing and the aerodynamic properties. The optical head consists of two optical systems. (1) The stereo-microscopic imager is composed of two CTAs placed downstream of two reflecting mirrors to image the detected particle, with a resolution down to 2.35 µm at two different viewing angles. The dual-imaging configuration produces two shadowgraphic images at two different angles for each detected particle. This provides an impression of the 3-D morphology in a similar way to that of the human ocular system. Reconstruction of a 3-D model for regular shapes, such as spheres, plates and columns is possible. (2) The polar nephelometer measures the polar scattered light from the cloud particle as it passes across a collimated laser beam. The angular resolution of the differential scattering function is 1° for the forward scattering direction (from 1 to 10°) and 8° for the side and backscattering di-

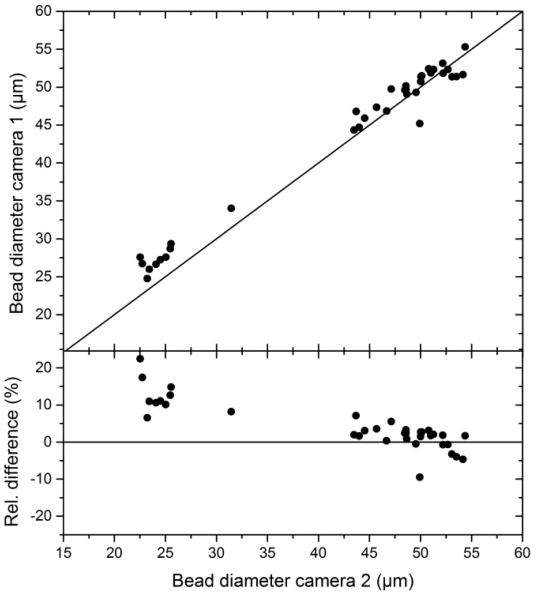

Figure 11. Comparison of the bead diameters deduced from the images of camera-telescope assembly 1 and 2.

rections (from 18 to 170°). The scattered signal is transmitted from the scattering plane to a multi-anode photomultiplier via PMMA optical fibres. Optical engineering calculations for light coupling between the PMMA fibre system and the multi-anode photomultiplier were presented in conjunction with laboratory characterization measurements. These results reveal a crosstalk between adjacent channels of up to 20 % that needs to be taken into account in the analysis of the polar nephelometer measurements. The crosstalk discussed here requires the application of a crosstalk correction factor to the PHIPS data based on a theoretical Mie scattering curve which limits the phase function data to Mie theory. Redesign of the coupling of the signal to the MAPMT started in order to eliminate the crosstalk in future measurements. Detailed signal detection and processing schemes were discussed. A comprehensive aerodynamic analysis was performed to investigate the mechanical stability of the probe and the possible turbulence at the detection volume. The crucial aerodynamic parameters (flow velocity, Mach number, pressure, temperature, turbulence) were discussed in detail under a variety of conditions to estimate the mechanical stability of the probe and to verify the geometry for a turbulence-free detection volume. Finally, we modelled the response and detection range of the scattering optics and demonstrated the measurement and crosstalk correction using standard glass beads.

As already mentioned above, the problem of crosstalk in the scattering signal requires a better optical design for the fibre MAPMT coupler. So far, the gain value of the MAPMT has only been changed manually by a mechanical potentiometer on the electronic board of the MAPMT. This is now replaced by a digitally controlled potentiometer to allow software access to the gain voltage. Another shortcoming of the MAPMT electronics is that the set gain value applies to all channels. Adjusting the gain to an optimum value which allows for detection at all channels, but prevents signal saturation at any of them, is difficult. An individual gain is required for each channel. The shattering of cloud particles at the inlet of the probe was not discussed in detail in Part I. It will be the subject of future work together with field measurements.

Acknowledgements. We express our gratitude to the technical and scientific staff of IMK-AAF for their continuous support until the achievement of the presented work goals. This work was funded within the Helmholtz Research Program Atmosphere and Climate and by the German Research Foundation (DFG grants SCHN 1140/1-1 and SCHN 1140/1-2) within the DFG priority program 1294 (HALO).

The article processing charges for this open-access publication were covered by a Research Centre of the Helmholtz Association.

Edited by: S. Malinowski
Reviewed by: D. Baumgardner and C. gurganus

References

Abdelmonem, A., Schnaiter, M., Amsler, P., Hesse, E., Meyer, J., and Leisner, T.: First correlated measurements of the shape and light scattering properties of cloud particles using the new Particle Habit Imaging and Polar Scattering (PHIPS) probe, Atmos. Meas. Tech., 4, 2125–2142, doi:10.5194/amt-4-2125-2011, 2011.

Baum, B. A., Yang, P., Hu, Y.-X., and Feng, Q.: The impact of ice particle roughness on the scattering phase matrix, J. Quant. Spectrosc. Ra., 111, 2534–2549, doi:10.1016/j.jqsrt.2010.07.008, 2010.

Baumgardner, D., Jonsson, H., Dawson, W., O'Connor, D., and Newton, R.: The cloud, aerosol and precipitation spectrometer: a new instrument for cloud investigations, Atmos. Res., 59–60, 251-264, doi:10.1016/S0169-8095(01)00119-3, 2001.

Bi, L., Yang, P., Kattawar, G. W., Hu, Y., and Baum, B. A.: Scattering and absorption of light by ice particles: Solution by a new physical-geometric optics hybrid method, J. Quant. Spectrosc. Ra., 112, 1492–1508, doi:10.1016/j.jqsrt.2011.02.015, 2011.

Bohren, C. F. and Huffman, D. R.: Introduction, in: Absorption and Scattering of Light by Small Particles, Wiley-VCH Verlag GmbH, 1–11, 2007.

Crépel, O., Gayet, J. F., Fournol, J. F., and Oshchepkov, S.: A new airborne Polar Nephelometer for the measurement of optical and microphysical cloud properties – Part II: Preliminary tests, Ann. Geophys., 15, 460–470, doi:10.1007/s00585-997-0460-0, 1997.

Draine, B. T. and Flatau, P. J.: Discrete-Dipole Approximation For Scattering Calculations, J. Opt. Soc. Am. A, 11, 1491–1499, doi:10.1364/josaa.11.001491, 1994.

Fugal, J. P., Shaw, R. A., Saw, E. W., and Sergeyev, A. V.: Airborne digital holographic system for cloud particle measure-

ments, Appl. Opt., 43, 5987–5995, doi:10.1364/ao.43.005987, 2004.

Gayet, J. F., Crépel, O., Fournol, J. F., and Oshchepkov, S.: A new airborne polar Nephelometer for the measurements of optical and microphysical cloud properties – Part I: Theoretical design, Ann. Geophys., 15, 451–459, doi:10.1007/s00585-997-0451-1, 1997.

Glen, A. and Brooks, S. D.: A new method for measuring optical scattering properties of atmospherically relevant dusts using the Cloud and Aerosol Spectrometer with Polarization (CASPOL), Atmos. Chem. Phys., 13, 1345–1356, doi:10.5194/acp-13-1345-2013, 2013.

Glen, A. and Brooks, S. D.: Single Particle Measurements of the Optical Properties of Small Ice Crystals and Heterogeneous Ice Nuclei, Aerosol Sci. Technol., 48, 1123–1132, doi:10.1080/02786826.2014.963023, 2014.

Havemann, S. and Baran, A. J.: Extension of T-matrix to scattering of electromagnetic plane waves by non-axisymmetric dielectric particles: application to hexagonal ice cylinders, J. Quant. Spectrosc. Ra., 70, 139–158, doi:10.1016/S0022-4073(00)00127-8, 2001.

Hesse, E., Mc Call, D. S., Ulanowski, Z., Stopford, C., and Kaye, P. H.: Application of RTDF to particles with curved surfaces, J. Quant. Spectrosc. Ra., 110, 1599–1603, doi:10.1016/j.jqsrt.2009.01.011, 2009.

Jourdan, O., Mioche, G., Garrett, T. J., Schwarzenböck, A., Vidot, J., Xie, Y., Shcherbakov, V., Yang, P., and Gayet, J.-F.: Coupling of the microphysical and optical properties of an Arctic nimbostratus cloud during the ASTAR 2004 experiment: Implications for light-scattering modeling, J. Geophys. Res.-Atmos., 115, D23206, doi:10.1029/2010jd014016, 2010.

Kaye, P. H., Hirst, E., Greenaway, R. S., Ulanowski, Z., Hesse, E., DeMott, P. J., Saunders, C., and Connolly, P.: Classifying atmospheric ice crystals by spatial light scattering, Opt. Lett., 33, 1545–1547, doi:10.1364/ol.33.001545, 2008.

Knollenberg, R. G.: The Optical Array: An Alternative to Scattering or Extinction for Airborne Particle Size Determination, J. Appl. Meteorol., 9, 86–103, doi:10.1175/1520-0450(1970)009<0086:TOAAAT>2.0.CO;2, 1970.

Korolev, A., Emery, E., and Creelman, K.: Modification and Tests of Particle Probe Tips to Mitigate Effects of Ice Shattering, J. Atmos. Oceanic Technol., 30, 690–708, doi:10.1175/jtech-d-12-00142.1, 2013.

Lawson, R. P., Baker, B. A., Schmitt, C. G., and Jensen, T. L.: An overview of microphysical properties of Arctic clouds observed in May and July 1998 during FIRE ACE, J. Geophys. Res.-Atmos., 106, 14989–15014, doi:10.1029/2000jd900789, 2001.

Lawson, R. P., O'Connor, D., Zmarzly, P., Weaver, K., Baker, B., Mo, Q., and Jonsson, H.: The 2D-S (Stereo) Probe: Design and Preliminary Tests of a New Airborne, High-Speed, High-Resolution Particle Imaging Probe, J. Atmos. Oceanic Technol., 23, 1462–1477, doi:10.1175/jtech1927.1, 2006.

Liu, C., Lee Panetta, R., and Yang, P.: The effects of surface roughness on the scattering properties of hexagonal columns with sizes from the Rayleigh to the geometric optics regimes, J. Quant. Spectrosc. Ra., 129, 169–185, doi:10.1016/j.jqsrt.2013.06.011, 2013.

Macke, A., Mueller, J., and Raschke, E.: Single Scattering Properties of Atmospheric Ice Crystals, J. Atmos. Sci., 53, 2813–2825, doi:10.1175/1520-0469(1996)053<2813:sspoai>2.0.CO;2, 1996.

Pruppacher, H. R. and Klett, J. D.: Microphysics of clouds and precipitation, 2 Edn., Atmospheric and oceanographic sciences library, Kluwer Academic Publishers, Dordrecht, 954 pp., 1997.

Schnaiter, M., Järvinen, E., Vochezer, P., Abdelmonem, A., Wagner, R., Jourdan, O., Mioche, G., Shcherbakov, V. N., Schmitt, C. G., Tricoli, U., Ulanowski, Z., and Heymsfield, A. J.: Cloud chamber experiments on the origin of ice crystal complexity in cirrus clouds, Atmos. Chem. Phys., 16, 5091–5110, doi:10.5194/acp-16-5091-2016, 2016.

Schön, R., Schnaiter, M., Ulanowski, Z., Schmitt, C., Benz, S., Möhler, O., Vogt, S., Wagner, R., and Schurath, U.: Particle habit imaging using incoherent light: a first step towards a novel instrument for cloud microphysics, J. Atmos. Oceanic Technol., 28, 439–512, doi:10.1175/2010jtecha1445.1, 2011.

Shcherbakov, V.: Why the 46° halo is seen far less often than the 22° halo?, J. Quant. Spectrosc. Ra., 124, 37–44, doi:10.1016/j.jqsrt.2013.03.002, 2013.

Shcherbakov, V., Gayet, J.-F., Baker, B., and Lawson, P.: Light Scattering by Single Natural Ice Crystals, J. Atmos. Sci., 63, 1513–1525, doi:10.1175/jas3690.1, 2006a.

Shcherbakov, V., Gayet, J.-F., Jourdan, O., Ström, J., and Minikin, A.: Light scattering by single ice crystals of cirrus clouds, Geophys. Res. Lett., 33, L15809, doi:10.1029/2006gl026055, 2006b.

Ulanowski, Z., Kaye, P. H., Hirst, E., Greenaway, R. S., Cotton, R. J., Hesse, E., and Collier, C. T.: Incidence of rough and irregular atmospheric ice particles from Small Ice Detector 3 measurements, Atmos. Chem. Phys., 14, 1649–1662, doi:10.5194/acp-14-1649-2014, 2014.

Vochezer, P., Järvinen, E., Wagner, R., Kupiszewski, P., Leisner, T., and Schnaiter, M.: In situ characterization of mixed phase clouds using the Small Ice Detector and the Particle Phase Discriminator, Atmos. Meas. Tech., 9, 159–177, doi:10.5194/amt-9-159-2016, 2016.

Weigel, R., Spichtinger, P., Mahnke, C., Klingebiel, M., Afchine, A., Petzold, A., Krämer, M., Costa, A., Molleker, S., Jurkat, T., Minikin, A., and Borrmann, S.: Thermodynamic correction of particle concentrations measured by underwing probes on fast flying aircraft, Atmos. Meas. Tech. Discuss., 8, 13423–13469, doi:10.5194/amtd-8-13423-2015, 2015.

Yang, P. and Liou, K. N.: Geometric-optics-integral-equation method for light scattering by nonspherical ice crystals, Appl. Opt., 35, 6568–6584, doi:10.1364/ao.35.006568, 1996.

Yang, P. and Liou, K. N.: T-Matrix Method and its Applications, in: Light scattering by nonspherical particles, edited by: Mishchenko, M. I. and Travis, L. D., Academic Press, New York, 173–221, 1999.

Yurkin, M. A. and Hoekstra, A. G.: The discrete dipole approximation: An overview and recent developments, J. Quant. Spectrosc. Ra., 106, 558–589, doi:10.1016/j.jqsrt.2007.01.034, 2007.